SSRG International Journal of Electrical and Electronics Engineering
ISSN: 2348-8379/ https://doi.org/10.14445/23488379/IJEEE-V11I12P111

Volume 11 Issue 12, 119-136, December 2024


*Original Article*

# Optimizing Solar and Wind Energy Integration in Grid-Connected EV Fast Charging Systems using Fuzzy Logic Control for Improved Stability and Power Quality

J. Srinu Naick[1], G. Chandra Sekhar[2], N.C. Kotaiah[3], Mallipeddi Anitha [4], B. Gopi Raja Naik [5]

[1]*Department of Electrical and Electronics Engineering, Chadalawada Ramanamma Engineering College, Andhra Pradesh, India.*
[2]*Department of Electrical and Electronics Engineering, GMR Institute of Technology, Andhra Pradesh, India.*
[3,4]*Department of Electrical and Electronics Engineering, R.V.R&J.C College of Engineering, Andhra Pradesh, India.*
[5]*Department of Electrical and Electronics Engineering, PNC&VIJAI Institute of Engineering and Technology, Andhra Pradesh, India.*

[1]*Corresponding Author : speaksrinu@gmail.com*

Received: 07 October 2024 Revised: 08 November 2024 Accepted: 06 December 2024 Published: 31 December 2024

***Abstract*** *- This paper presents the complete approach to integrating solar and wind renewable energy sources into grid-connected Electric Vehicle (EV) quick charging systems. The solar system utilizes a Perturb and Observe (P&O) Maximum Power Point Tracking (MPPT) boost converter to maximize energy extraction from the photovoltaic panels. In contrast, the wind energy system employs a similar MPPT technique to maximize wind power consumption. The proposed fuzzy logic controller system ensures consistent and efficient power conversion management during EV charging activities, improving system stability. Neutral-Point Clamped (NPC) voltage source converters are further utilised to optimise power conversion, improve voltage balance, and reduce switching losses. Reducing voltage fluctuations and resolving power quality issues helps the fuzzy logic controller significantly increase system stability. MATLAB simulations show that the combined use of MPPT for solar and wind, fuzzy logic control, and NPC converters results in effective energy distribution, enhanced load balancing, and reduced Total Harmonic Distortion (THD). Apart from fast-charging electric vehicles, the system is supposed to manage residential linear and nonlinear loads. The findings imply that whilst preserving power grid stability and improving general system performance for different load types, this integrated system successfully allows large-scale EV rapid charging utilising renewable energy.*

***Keywords*** *- Electrical vehicles, Fuzzy Logic Controller (FLC), Harmonics distortion, Power quality, Renewable energy, Neutral-Point Clamped (NPC) converters, Magnetic linked converter.*

## 1. Introduction

Rising energy demand is driving strain on the ageing power infrastructure worldwide, squeezing governments, businesses, and consumers as electricity prices climb. Burning fossil fuels and air pollution from two of the most widely utilized traditional energy sources create health problems. Among other renewable energy sources, solar and wind power might assist in lowering operating and maintenance costs, peak demand, and environmental effects, therefore addressing these concerns [1, 2]. Fuel and maintenance costs might be paid during the lifetime of investments in renewable energy infrastructure [3, 4]. Energy-efficient technologies and methods could cut the financial cost of generating electricity and energy usage. Electric vehicles (EVs) are better for the environment than petrol vehicles as they reduce pollutants and greenhouse gas emissions [5, 6]. There are several advantages to integrating RES into utilities, including increased power system flexibility, less power loss, and decreased environmental pollution [7]. However, an increasing number of technical problems have been raised by RES. One such problem that must be handled is islanding operation [8]. It is one of the major issues. When a section of the distribution network is cut off from the utility grid, but the local Distributed Generation (DG) units continue to supply the loads, this phenomenon is known as islanding [9]. This capacity ensures the reliability of EV charging as well as the continuous stability of the power supply for home loads comprising both linear and nonlinear devices [10]. By distributing sources and giving renewable options first importance, we can create a stronger and fairly priced energy system [11]. Integrating renewable energy sources and electric automobiles into a grid-connected system addresses economic and environmental issues, even as the grid-support qualities of the system increase dependability and stability, therefore

supporting a sustainable future [12]. Among renewable energy sources, sun and wind are ones whose efficiency can suffer should weather patterns reduce their power production. Maximum Power Point Tracking (MPPT) techniques are often used to increase the power extraction from many sources [13]. Whereas the boost converter raises the voltage from solar panels to meet load or grid demands in solar energy systems, the P&O algorithm routinely adjusts the operational voltage of solar panels to assure optimal power point performance [14]. This approach ensures that the system constantly finds the appropriate power point regardless of outside factors like solar intensity and temperature [15].

By varying its operating position in response to wind speed changes, MPPT helps the turbine's wind energy-producing systems function optimally [16]. One may do this using a power electronic converter or adjusting the blade pitch. In systems operating a Permanent Magnet Synchronous Generator (PMSG), the MPPT technique modulates the electrical demand of the generator, therefore controlling the rotor speed and ensuring the turbine works at the appropriate tip-speed ratio [17]. Wind energy systems use three primary MPPT techniques: Tip Speed Ratio (TSR), Power Signal Feedback (PSF), and Hill Climb Search (HCS) [18]. While TSR control maintains a steady link between turbine rotor speed and wind velocity, PSF control uses known power curves to adjust the operating point. The HCS method detects subsequent power variations and modulates control in accordance with tiny changes to the operational point [19]. Integrating renewable energy into grid-connected or independent systems using MPPT approaches can ensure optimal power generation despite unfavourable climatic conditions. Permanent Magnet Synchronous Generators (PMSGs) are widely used in wind power-producing systems to produce AC electricity.

This is then converted into DC for integration with energy storage systems or grid-connected systems. Both PMSG wind turbines and grid-side converters make great use of Neutral-Point-Clamped (NPC) Voltage Source Converters (VSCs) because of their performance benefits [20]. Two advantages of the three-level NPC converter over conventional two-level inverters are less switching stress and lower harmonic distortion in the output voltage [21]. This notably applies to high-power applications such as FACTS, motor drives, and active power filters. Still, the main challenge with this design is balancing the neutral-point voltage. Under ideal conditions, every capacitor should hold half of the DC bus voltage, ensuring flawless performance [22]. By current flowing beyond the neutral point, the real-world operation might cause voltage swings across the capacitors, therefore creating an imbalance capable of generating low-frequency harmonics in the output voltage. Therefore, capacitor voltage balancing control is a critical area of research and development for three-level NPC inverters to ensure system stability and protect switching devices under various operating conditions [23]. These days, voltage source converters (VSC) based on bidirectional multipurpose EV charging and domestic loads approach are somewhat common [24]. Solar PV and wind-based renewable energy sources are mostly connected to the DC bus, which enables these electric chargers. Consequently, studies on RES-powered electric vehicle charging have recently attracted much interest [25]. In many spheres, power electronics have been used to use renewable energy in the conventional power grid, home loads applications, and EV charging applications. While an electric vehicle may be charged using conventional power electronics such as buck converters and boost converters, their efficiency cannot be guaranteed. Inadequate energy management skills are another main problem with buck/boost converters [26].

Researchers have investigated alternative solutions such as conventional buck/boost converters, especially for onboard charging stations, which suffer from poor energy consumption, for example, which is crucial for energy production from an electric vehicle's perspective [27]. Furthermore, traditional converters have some constraints, including the usual rectifier bridge encountering high voltage stress and high circulation current in the freewheeling period [27]. The drawbacks of current converters, such as lack of galvanic isolation and input/output current/voltage range constraints, remain unresolved. To address these issues, a new type of converter, magnetic-linked power converters (MLPC), has gained popularity in the power sector due to their various applications. Introduced in the 1980s, the magnetic-linked power converter has a dual active bridge [26]. Then, it became quite popular in the 1990s [26]. Comparing the magnetically linked converter with other DC-to-DC converters, it features such as the ability of high-power handling with less power loss in power conversion, galvanic isolation (GI) between the input and output circuitries, cost-efficiency of the components due to the rather simpler design, and high efficiency concerning power transmission.

The magnetic-linked converter, first introduced in 1991, has evolved to suit various applications, including electric vehicle charging and renewable energy integration. Its diverse topologies have been developed for various applications, including solar and wind power generation. However, these fluctuations can cause instability in the electrical system, affecting the ability to provide a constant and reliable supply. The first magnetic-linked converter was designed for dual active bridge arrangements and has since evolved to accommodate various applications. The proposed system describes non-linear control schemes based on sliding mode control [28], artificial intelligent control [29, 30], robust control [31], adaptive control [32], backstepping control [33], and many more to solve these challenges. All of the following improve system performance at various implementation complexities. Artificial intelligence technologies, such as Fuzzy Logic Control (FLC), perform better dynamically for nonlinear systems with less dependence on system

characteristics. Despite being computationally demanding and requiring more memory than PI control, CPU technological advances have made this a less significant restriction. The proposed system handles these challenges using Fuzzy Logic Controllers (FLCs) [34]. More effectively than conventional controllers like PI, FLCs can regulate uncertainty in power generation and nonlinearities in output.

They dynamically change control settings to provide stability even in quick variations in power demand depending on grid, renewable, load data, and grid input [35]. Fuzzy logic controllers reduce Total Harmonic Distortion (THD), therefore improving power quality and perhaps creating inefficiencies in power supply, overheating of electrical components, and shorter lifespan of grid-connected equipment. Reducing THD assures a more constant power supply to household loads and electric vehicles, therefore improving efficiency and protecting sensitive equipment from voltage spikes and waveform distortions. Fuzzy logic controllers increase grid stability by changing power flow between renewable sources, the grid, and loads to lower volatility and imbalances [36]. This combination of grid stability and power quality improvement provides reliability in handling modern energy consumption and strengthens and improves efficiency.

## 2. Proposed System Configuration

Rapid charging of grid-connected Electric Vehicles (EV) combines solar and wind energy sources in order to ensure efficient energy management and power quality improvement, as shown in Figure 1. Comprising a Photovoltaic (PV) array paired to a Perturb and Observe (P&O) Maximum Power Point Tracking (MPPT), the solar energy system maximises energy extraction. Similarly, the wind energy system makes the best use of wind power by means of an MPPT controller.

Both sources are coupled to a shared DC bus supplying into the grid using Neutral-Point Clamped (NPC) converters, which improve power conversion efficiency, reduce switching losses, and preserve voltage balance. Fuzzy logic controllers control power flow, improve stability, and maintain voltage levels throughout home load operation and EV charging all across the system. The controllers handle power quality issues, including voltage fluctuations and reduce Total Harmonic Distortion (THD) by assisting in governing energy distribution among the solar, wind, and grid sources. By supporting both linear and nonlinear residential loads, the system ensures stability and efficient load balancing, thereby allowing fast EV charging.

## 3. Modeling and Designing of Proposed System Configuration

### *3.1. Wind Turbine Design*

The wind turbine is the foundational component of a wind energy system; it converts the wind's kinetic energy into mechanical power. The rotor's size, the wind's velocity, the shape of the blades, and other factors all influence how efficient this energy collection is.

#### *3.1.1. Power Output of a Wind Turbine*

The formula for the mechanical power (P) generated by a wind turbine is:

$$P = \frac{1}{2} \cdot \rho \cdot A \cdot V^3 \cdot C_p \quad (1)$$

Where: P = Mechanical power captured by the turbine (in watts), ρ = Air density (1.225 kg/m3), A = Swept area of the rotor (in square meters), A=πR2, where R is the radius of the rotor, V = Wind speed (in m/s), $C_P$ = Power coefficient (efficiency of the turbine), typically ranging from 0.35 to 0.45.

The maximum possible value is 0.59 (Betz limit). Wind turbines harness the power of the wind's kinetic energy and turn it into mechanical force. Since wind turbines produce a disproportionately large amount of electricity in response to increases in wind speed, the wind's kinetic energy grows exponentially with increases in wind speed. Unfortunately, not all of the wind's kinetic energy can be harnessed; the efficiency of energy conversion is determined by the power coefficient $C_p$ Capturing more than 59% of the kinetic energy of the wind is impossible according to the Betz limit. Because it controls the amount of wind energy that reaches the turbine, the rotor's swept area is crucial. A greater amount of electricity may be collected by expanding the swept area.

#### *3.1.2. Rotor Diameter and Swept Area*

The area that the spinning blades cover, or the swept area A, is what decides the amount of wind energy that can be captured:

$$A = \pi R^2 \quad (2)$$

Where: R = Rotor radius (in meters).

The turbine can pick up more wind energy if the rotor is bigger. Large wind turbines with larger blades may produce more electricity even at reduced wind speeds. Altering the blade length significantly impacts power generation because the swept area grows in direct proportion to the square of the rotor radius.

#### *3.1.3. Tip Speed Ratio (TSR)*

The tip speed ratio (λ) is the blade tip speed to wind speed ratio:

$$\lambda = \frac{\omega \cdot R}{V} \quad (3)$$

Where: ω = Angular velocity of the rotor (in radians per second), R = Rotor radius (in meters), V = Wind speed (in meters per second). In order to maximise the efficiency of the turbine, the tip speed ratio is crucial. There is a sweet spot for the ratio of blade speed to wind speed that is unique to each wind turbine design. A lack of energy capture occurs when the blades move at a snail's pace. They lose efficiency and cause drag if they move too fast.

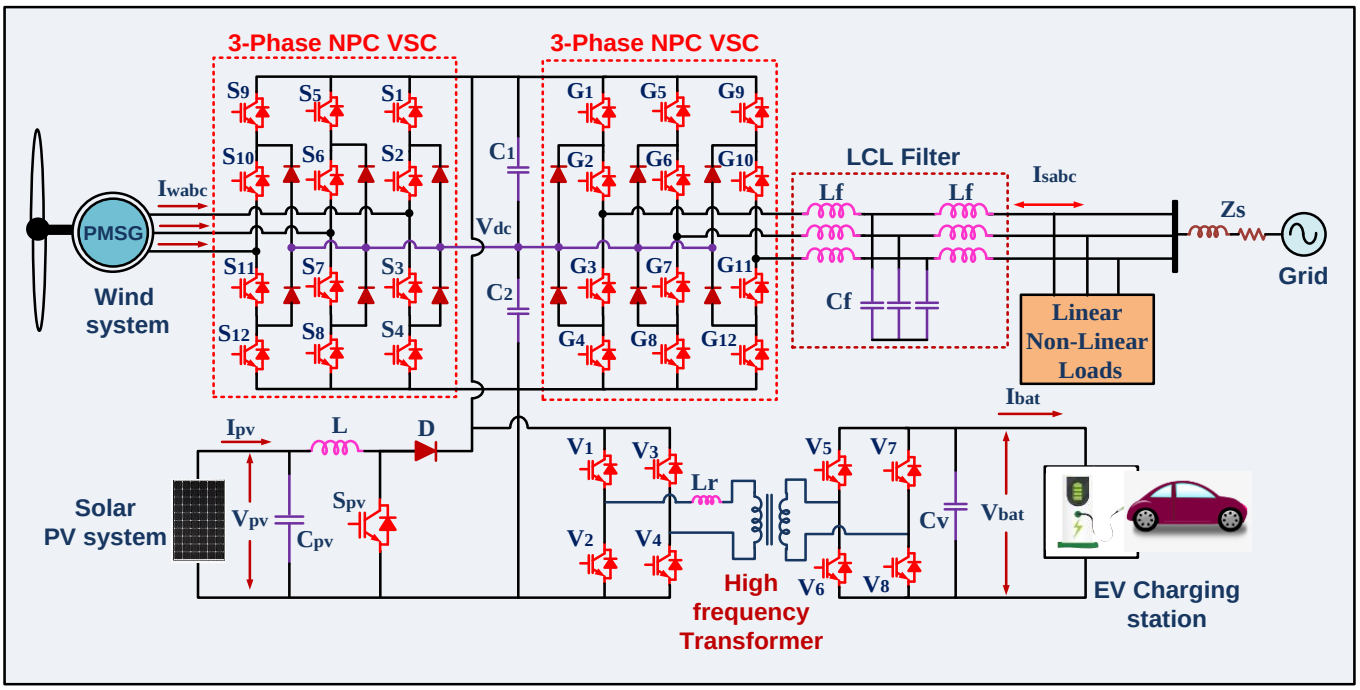


**Fig. 1 Proposed system configuration**

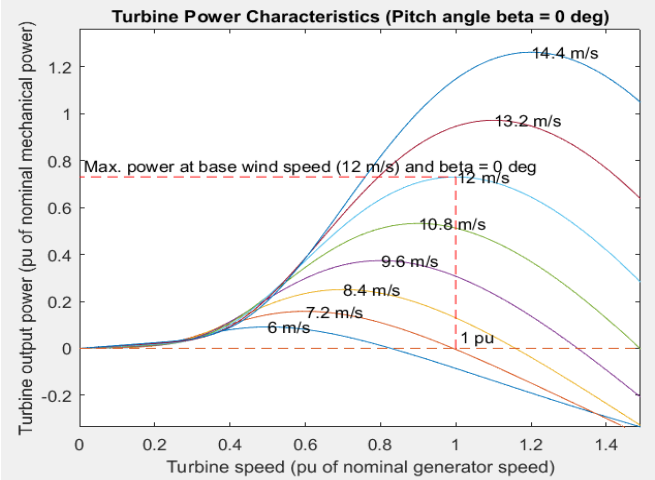


**Fig. 2 Turbine power $P_t$ function for varying wind speed $\omega_r$ by rotational speed**

### *3.1.4. Mechanical Torque on the Rotor*

The mechanical torque (T) on the wind turbine rotor is the force that causes the rotor to spin and can be calculated using:

$$T = \frac{P}{\omega} \quad (4)$$

Where: T = Torque (in Nm), P = Mechanical power (in watts), ω = Angular velocity (in radians per second). Torque is the twisting force that drives the rotor's motion. As the rotor extracts energy from the wind, this mechanical energy is transmitted to the generator, which is converted into electrical power. Torque is inversely proportional to the angular velocity: the turbine generates less torque at high speeds, and vice versa.

### *3.2. Two-Mass Drive Train model*

The two-mass drive train model is widely used in wind energy conversion systems (WECS) for transient stability analysis because it offers a more accurate representation of the mechanical dynamics than the simpler one-mass model. The two-mass model divides the system into two key parts: the turbine and the generator, which are connected via a flexible shaft.

### *3.2.1. Turbine Dynamics*

An appropriate differential equation to describe the wind turbines' mechanical dynamics is:

$$J_t \cdot \frac{d\omega_t}{dt} = T_t - K_s \cdot (\theta_t - \theta_g) - D_s \cdot (\omega_t - \omega_g) \quad (5)$$

Where: $J_t$ = Moment of inertia of the turbine (kg·m²), $\omega_t$ = Angular speed of the turbine (rad/s), $T_t$ = Mechanical torque from the turbine (Nm), $K_s$ = Shaft stiffness (Nm/rad), $D_s$ = Shaft damping coefficient (Nms/rad), $\theta_t$ = Angular position of the turbine (rad), $\theta_g$ = Angular position of the generator (rad), $\omega_g$ = Angular speed of the generator (rad/s). This equation represents the mechanical dynamics of the rotor of a wind turbine. The angular acceleration and turbine inertia are affected by the following factors: shaft stiffness and damping, turbine torque ($T_t$), and the difference in angular position and speed between the generator and the turbine.

### *3.2.2. Generator Dynamics*

The mechanical dynamics of the generator are similarly represented by:

$$J_g \cdot \frac{d\omega_g}{dt} = K_s \cdot (\theta_t - \theta_g) - D_s \cdot (\omega_t - \omega_g) - T_g \quad (6)$$

Where: $J_g$ = Moment of inertia of the generator (kg·m²), $\omega_g$= Angular speed of the generator (rad/s), $T_g$ = Electromagnetic torque produced by the generator (Nm). This equation governs the generator's mechanical dynamics, considering the torque transmitted from the flexible shaft $K_s(\theta_t-\theta_g)$ and the shaft's damping effect $D_s(\omega_t-\omega_g)$. The electromagnetic torque $T_g$ opposes the mechanical torque, representing the electrical load.

*3.2.3. Shaft Dynamics*

The following relationships explain the shaft dynamics between the generator and the turbine:

$$\frac{d\theta_s}{dt} = \omega_t - \omega_g \quad (7)$$

$$\frac{d\theta_g}{dt} = \omega_g \quad (8)$$

Where: $\theta_s$ = Shaft twist angle (rad)

The relative difference influences the shaft twist angle in angular velocity between the turbine and the generator. This twist, along with the shaft stiffness and damping, determines how torque is transferred between the turbine and generator.

### *3.3. Permanent Magnet Synchronous Generators Used in Wind Energy Conversion Systems*

A permanent magnet synchronous generator (PMSG) has several uses and is used in wind energy conversion systems (WECS).

- High power density: PMSGs provide more power per unit volume compared to other generators.
- High efficiency: With no rotor copper losses (since no external excitation is required), PMSGs have a higher efficiency.
- Absence of a gearbox: PMSGs can operate directly with the turbine without needing a gearbox, reducing mechanical complexity and maintenance needs.

The PMSG's transient behavior in WECS may be studied by using the Park transformation, which simplifies the study by reducing the three-phase system to a two-dimensional (d and q-axis) model that spins at the rotor speed. The d-q reference frame is another name for this transition. By using the d- and q-axis components, the dynamic equations of the PMSG may be defined in the dq reference frame.

*3.3.1. Electromagnetic Torque Equation*

An essential component of the PMSG, the electromagnetic torque $T_e$ is produced when the stator currents and rotor magnetic field interact. The electromagnetic torque in the d-q reference frame is given by:

$$T_e = \frac{3}{2}P \cdot \left(\lambda_f \cdot i_q + \left(L_d - L_q\right) \cdot i_d \cdot i_q\right) \quad (9)$$

Where: $T_e$ = electromagnetic torque (Nm), P = number of pole pairs, $\lambda_f$ = flux linkage due to permanent magnets ($wb$), $i_d, i_q$= d-axis and q-axis currents (A), $L_d, L_q$ = d-axis and q-axis inductances (H).

*3.3.2. Mechanical Dynamics: Torque and Speed Relationship*

The mechanical dynamics of the PMSG are described by the equation of motion, which relates the mechanical torque from the wind turbine to the electromagnetic torque produced by the generator:

$$J \cdot \frac{d\omega_m}{dt} = T_m - T_e - B \cdot \omega_m \quad (10)$$

Where: J = moment of inertia of the rotor (kg·m²), $\omega_m$ = mechanical angular velocity of the rotor (rad/s), $T_m$ = mechanical torque from the wind turbine (Nm), $T_e$ = electromagnetic torque generated by the PMSG (Nm), B = friction coefficient (Nms/rad)

*3.3.3. Power Equations*

The generator's output power is given by the product of the voltage on the q-axis and the current in the d-q reference frame:

$$P_{elec} = \frac{3}{2}\left(v_d \cdot i_d + v_q \cdot i_q\right) \quad (11)$$

A relationship exists between the mechanical power that the wind turbine transfers to the PMSG and the rotor speed and torque:

$$P_m = T_m \cdot \omega_m \quad (12)$$

The mechanical power input and electrical power output may be used to evaluate the efficiency of the PMSG.

## 4. Design and Configuration of Solar PV System

### *4.1. Single-Diode Solar PV Model*

To design a solar PV model with a single diode, one must first study the electrical properties of the PV cell. For the purpose of simulating PV cell behavior, the single-diode model is among the most popular choices. According to Figure 3, this model incorporates a current source, a single diode, and series and shunt resistances to symbolise losses.

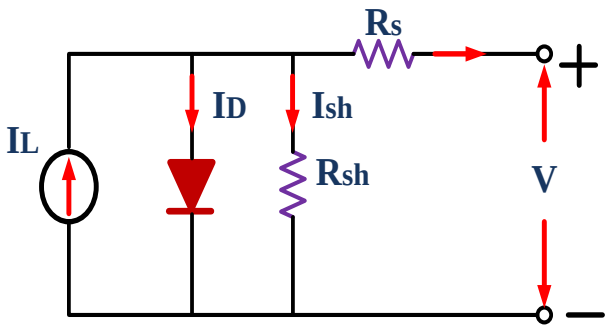


**Fig. 3 Equivalent model of PV solar**

### *4.2. Basic Equation of the Single-Diode Model*

The equation that governs the behavior of the single-diode PV model is derived from Kirchhoff's current law (KCL):

$$I = I_{Ph} - I_D - I_{sh} \quad (13)$$

Where: I = output current of the PV module (A), $I_{Ph}$= photocurrent, the current generated by light (A), $I_D$ = diode current (A), $I_{sh}$= shunt current (A)

#### *4.2.1. Diode Current ($I_D$)*

The current through the diode is described by the Shockley diode equation:

$$I_D = I_0\left(e^{\frac{V+IR_S}{nV_t}} - 1\right) \quad (14)$$

Where: $I_0$ = reverse saturation current of the diode (A), V = voltage across the PV cell (V), $R_s$ = series resistance (Ω), n = diode ideality factor (typically between 1 and 2), $V_t$ = thermal voltage (V), given by $V_t$=qkT Here: k = Boltzmann constant ($1.38 \times 10^{-23}$ J/K), T = temperature in Kelvin (K), q = electron charge ($1.6 \times 10^{-19}$ C)

#### *4.2.2. Shunt Current ($I_{sh}$)*

The current through the shunt resistance $R_{sh}$ is modeled as:

$$I_{sh} = \frac{V+IR_S}{R_{sh}} \quad (15)$$

### *4.3 Equation of the Single-Diode PV Model*

By substituting the expressions for $I_D$ and $I_{sh}$into the main current equation, we get the complete form of the single-diode model:

$$I = I_{Ph} - I_0\left(e^{\frac{V+IR_S}{nV_t}} - 1\right) - \frac{V+IR_S}{R_{sh}} \quad (16)$$

#### *4.3.1. Photocurrent ($I_{Ph}$)*

The temperature has an effect on the amount of light that reaches the cell, which in turn affects the amount of current that the cell generates as a result of light. This might be represented as:

$$I_{ph} = \left[I_{ph,ref} + \mu I_{Ph} \cdot (T - T_{ref})\right] \cdot \frac{G}{G_{ref}} \quad (17)$$

Where: $I_{ph,ref}$ = reference photocurrent at standard test conditions (STC), $I_{Ph}$ = temperature coefficient of photocurrent (A/°C), T = cell temperature (°C), $T_{ref}$ = reference temperature (usually 25°C), G = irradiance (W/m²), $G_{ref}$ = reference irradiance at STC (1000 W/m²)

#### *4.3.2. Saturation Current ($I_0$)*

The reverse saturation current varies exponentially with temperature:

$$I_0 = I_{0,ref}\left(\frac{T}{T_{ref}}\right)^3 e^{\frac{Eg}{nV_t}\left(\frac{1}{T_{ref}} - \frac{1}{T}\right)} \quad (18)$$

Where: $I_{0,ref}$ = reverse saturation current at reference temperature, $E_g$ = bandgap energy of the semiconductor (typically 1.1 eV for silicon)

### *4.4. Open Circuit Voltage and Short Circuit Current*

#### *4.4.1. Short Circuit Current ($I_{sc}$)*

When the terminals of the PV cell are shorted, the current is maximum and equal to the photocurrent:

$$I_{sc} \approx I_{Ph} \quad (19)$$

This approximation holds because the diode and shunt current contributions are small under short-circuit conditions.

#### *4.4.2. Open Circuit Voltage ($V_{OC}$)*

When the terminals are open, no current flows through the PV cell. Setting I=0 in the diode equation gives:

$$V_{oc} = nV_t \ln\left(\frac{I_{ph}}{I_0} + 1\right) \quad (20)$$

This equation shows that the open-circuit voltage depends logarithmically on the photocurrent and the reverse saturation current.

In solar energy systems, a solar PV boost converter is often used to maximise power extraction from a photovoltaic (PV) array and increase the voltage to the required level. This converter is equipped with the Perturb and Observe (P&O) MPPT algorithm, as seen in Figure 4.

With these two components working together, the PV array may send its energy directly to the load or EV batteries.

### *4.5. Boost Converter for Solar PV*

A boost converter is a kind of DC-DC converter that may raise the output voltage from the PV array's input voltage.

An essential component of photovoltaic (PV) systems, the boost converter increases the voltage supplied to the load and enables the PV array to achieve its maximum power point (MPPT).

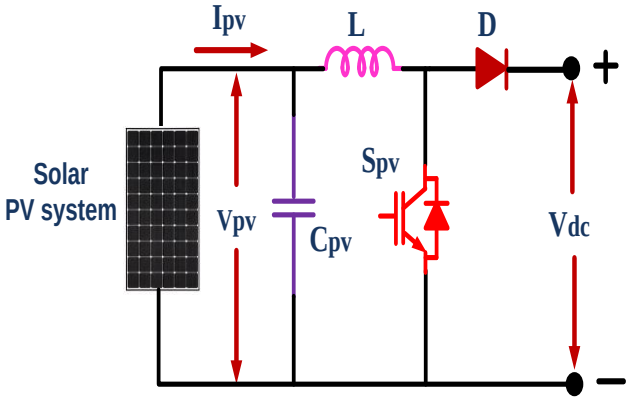


**Fig. 4 solar PV boost converter**

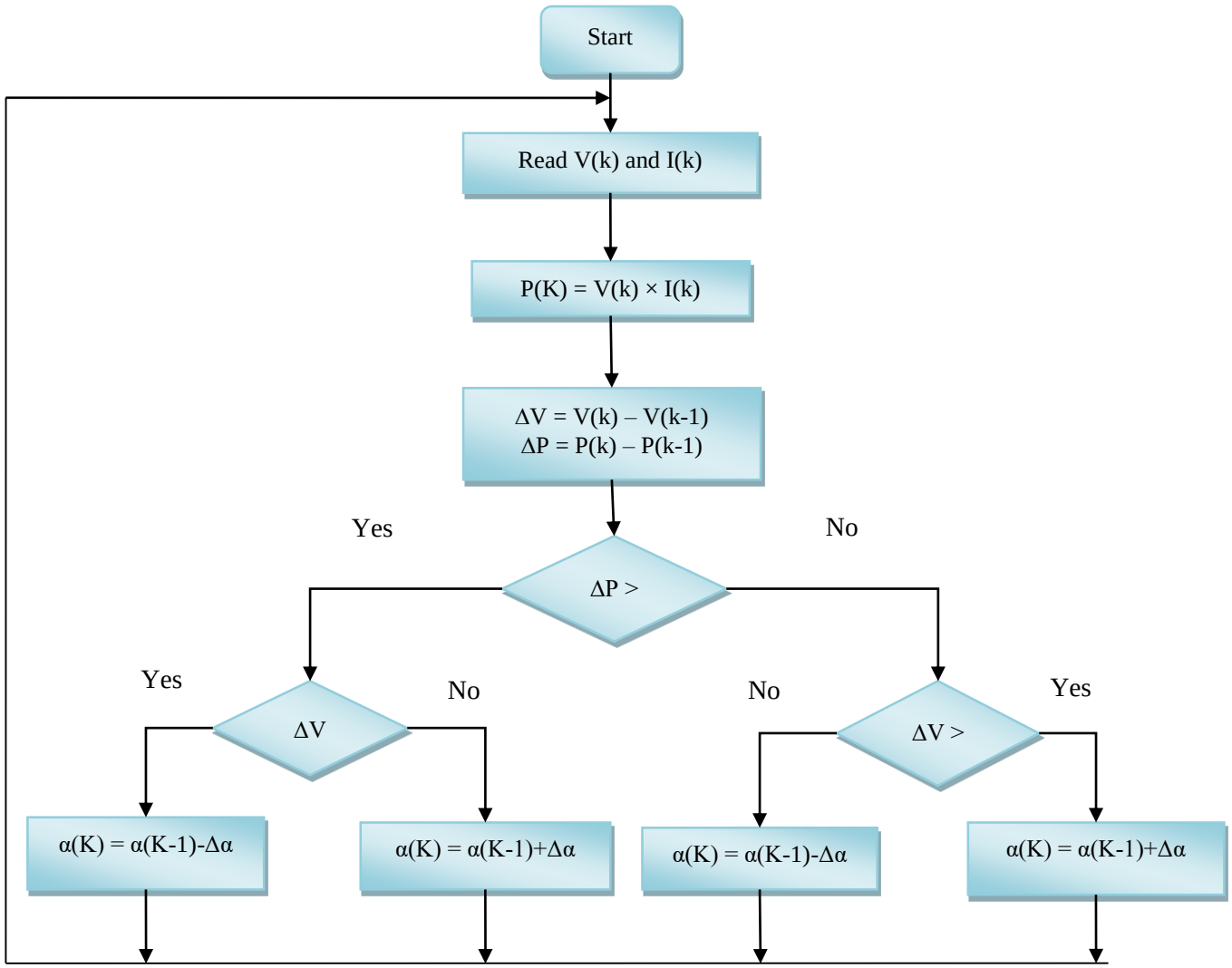


**Fig. 5 Flow chart of P&O MPPT algorithm**

A boost converter's "on" state is essentially a closed switch, and its "off" state is a rise in the output voltage caused by energy being released from an inductor. The following formula controls the relationship between $V_{in}$ (the input voltage) and $V_{out}$ (the output voltage) for any certain boost converter:

$$V_{out} = \frac{V_{in}}{1-D} \quad (21)$$

Where: The output voltage, $V_{out}$, is equal to the input voltage $V_{in}$, which comes from the PV array. The duty cycle, denoted as D, is the percentage of the switching period when the switch is closed. The MPPT algorithm controls the duty cycle D to ensure the PV array works at its maximum power point tracking (MPPT), which in turn determines the voltage step-up. The P&O MPPT method uses a solar PV boost converter to optimise power extraction by continuously adjusting the operating voltage of the PV array. This technology enhances the variable DC voltage from the PV array to a higher, usable level based on the load or EV battery requirements. The P&O approach controls the boost converter's duty cycle by varying the operating voltage and monitoring the resulting change in power output, as shown in Figure 5. The input voltage is initially perturbed, either increased or decreased, by the converter's duty cycle.

Should the resultant power rise, the perturbation proceeds in the same direction; should the power drop, the algorithm flips the perturbation's direction. The P&O algorithm guarantees that the PV array runs close to the Maximum Power Point (MPP), which is necessary for optimising energy collection under different environmental circumstances, including irradiation and temperature, by always changing the voltage. The boost converter subsequently delivers optimum efficiency in energy transmission by converting the optimal voltage from the PV array to a higher output voltage that satisfies the system's needs. This real-time tracking and conversion mechanism improves solar energy systems' efficiency and performance.

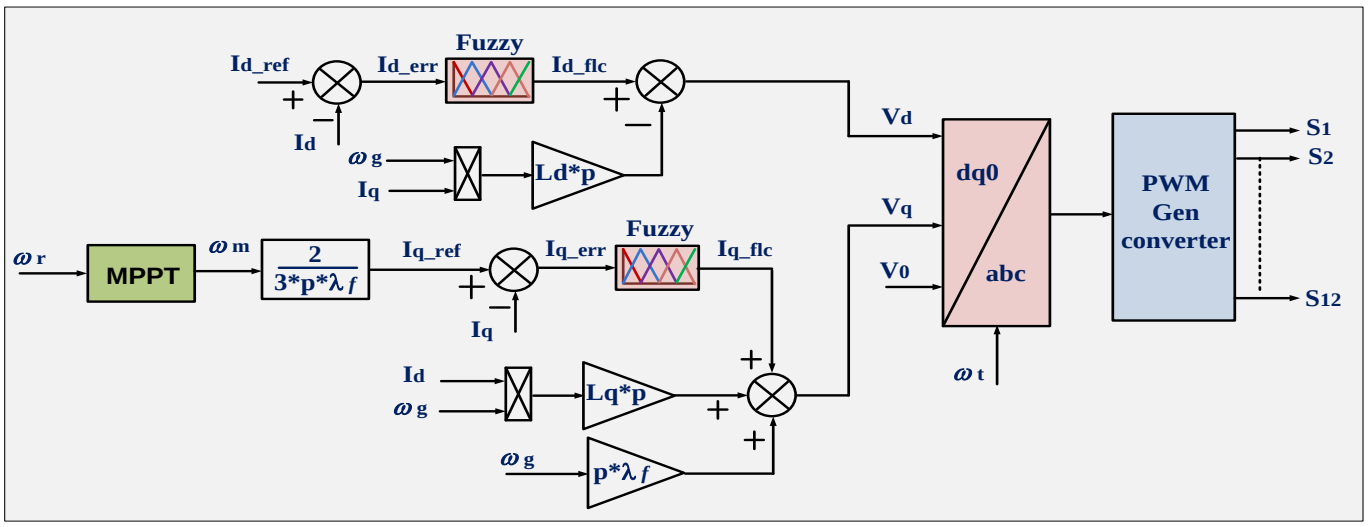


**Fig. 6 A schematic of the active rectifier-based voltage source conversion system for wind energy NPCs based on PMSG**

## 5. Controller Designing of Proposed System

### *5.1. Machine Side Control*

The machine-side control relies heavily on wind speed reference generation to get the most power out of the wind turbine. In Figure 6, we can see the control diagram of an active rectifier-connected PMSG.

The ideal ratio of tip speed to actual wind speed determines the reference rotor speed. The control algorithm uses the reference torque derived from the reference speed to manage the wind turbine power output. This method guarantees effective energy harvesting from different types of wind. The reference voltage $V_q^*$ represented for machine side controller

$$\omega_m = \frac{\lambda_{opt}\omega_r}{R} \tag{22}$$

Where $\omega_m$ is represents reference rotor speed
The q-axis current reference $I_{q\_ref}$ is:

$$i_{q\_ref} = \frac{2\cdot\omega_m}{3\cdot P\cdot\lambda_f} \tag{23}$$

Where $\omega_m$= reference rotor speed, P = number of pole pairs, $\lambda_f$ = flux linkage due to permanent magnets ($wb$)

$$i_{q-err} = \dot{i}_{q\_ref} - i_q \tag{24}$$

The reference voltage is generated by an inner loop current controller, which controls the machine-side converter. The d-q axis is referenced by the following:

$$V_q^* = \dot{i}_{q-flC} + i_d \cdot \omega_g \times L_q \cdot P + \omega_g \times P \cdot \lambda_f \tag{25}$$

Where $I_{q\_flC} = i_q$ current controlled by fuzzy logic controller, $i_q, i_d$ = generator stator current, $\omega_g$= generator speed, P = number of pole pairs, $\lambda_f$ = flux linkage due to permanent magnets ($wb$)The reference voltage $V_d^*$ represented the machine-side controller

$$i_{d\_err} = \dot{i}_{d\_ref} - i_d \tag{26}$$

$$V_d^* = \dot{i}_{d\_flC} + i_d \cdot \omega_g \times L_q \cdot P \tag{27}$$

Where $V_d^*, V_q^*$ represent reference machine voltage in the *d-q* axis; $i_q, i_d$ represent reference stator current in the *d-q* axis; System control efficiency is of the utmost importance in wind power generation, especially for PMSGs. The procedure starts by applying the Park transformation on three-phase AC currents and voltages to convert them into the d-q reference frame. This optimises performance by adjusting the torque and flux components, simplifying machine operation. The inverse Park transformation changes these voltage references back into three-phase AC voltage references after the necessary voltage has been calculated. The three-phase active rectifier on the machine side is controlled by switching signals generated by a Pulse Width Modulation (PWM) generator, which is supplied with these voltage references. In order to manage the power flow from the wind turbine, this accurately regulates the rectifier's switching. This allows for excellent machine control and maximum power extraction efficiency, regardless of the wind conditions.

### *5.2. Grid Side Control*

A Voltage Source Converter (VSC) installed on the grid may link DC energy sources like solar panels and wind turbines to a charging station for electric vehicles. The VSC converts DC power into AC, feeding the grid and supplying the EV charging system. The hysteresis current control technique regulates the VSC by maintaining the grid current within a predefined hysteresis band, ensuring fast dynamic response and accurate current tracking, as shown in Figure 7. This method improves power quality and reduces Total Harmonic Distortion (THD), enabling efficient integration of renewable energy with EV charging, ensuring stability and performance under varying generation and load conditions.

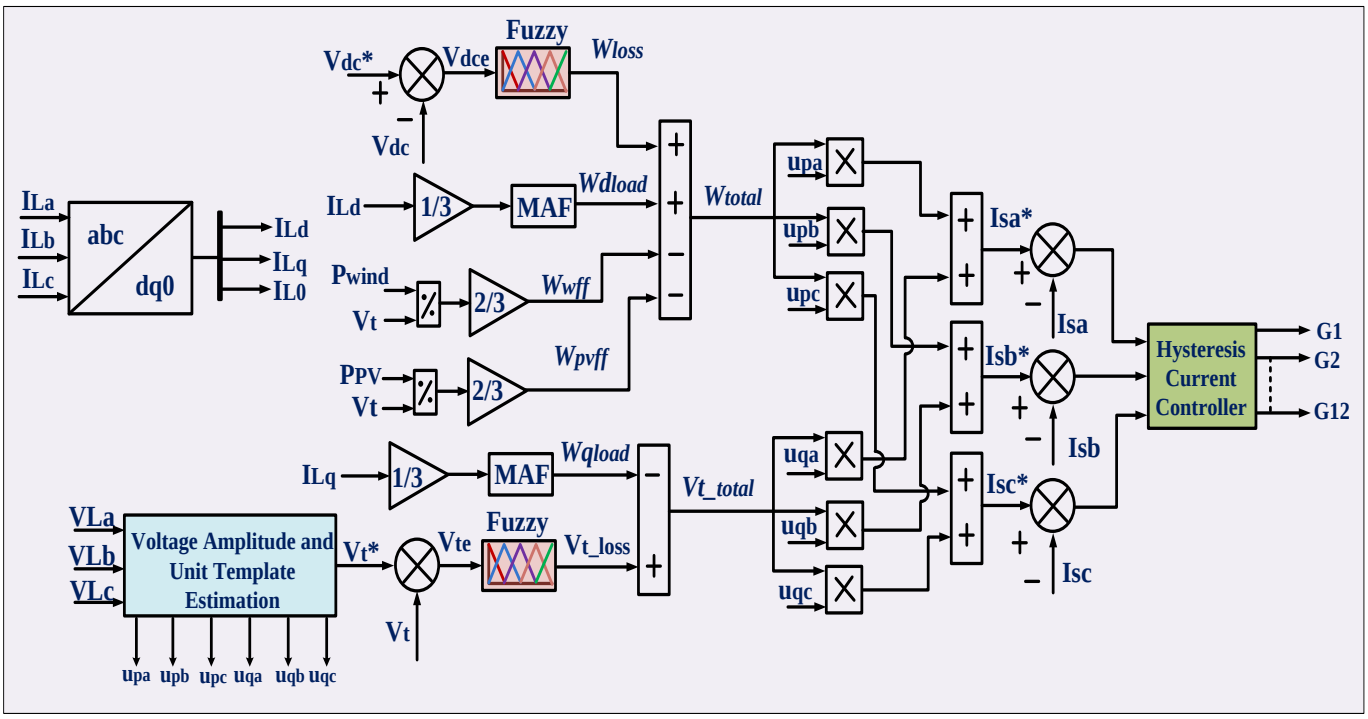


**Fig. 7 Control diagram of bidirectional AC-DC NPC voltage source converter**

*5.2.1. DC Loss Component Estimation*

An Electric Vehicle (EV) charging system that incorporates solar and wind energy is designed using a DC link voltage controller using a Fuzzy Logic Controller (FLC). The FLC regulates the DC link voltage, ensuring stable power delivery despite variations in renewable energy generation. The controller adjusts the Voltage Source Converter (VSC) at the grid side by adjusting the error between the reference and actual DC link voltage. The fuzzy logic controller processes this error using fuzzy rules and membership functions to generate appropriate control signals for the VSC, maintaining the desired DC link voltage and ensuring reliable charging for EVs.

$$V_{dce} = V_{dc}^{*} - V_{dc} \tag{28}$$

*5.2.2. Estimation of Feed-Forward Components of RERs*

The DC link voltage control system's dynamic response is enhanced using feed-forward terms linked to Renewable Energy Resources (RERs), such as solar and wind. These terms are calculated based on real-time power output, allowing the controller to anticipate changes in power flow to the DC link. These terms are derived from monitoring variations in solar irradiance and wind speed, which directly impact the power generated by solar panels and wind turbines.

By incorporating these terms into the control strategy, the system can preemptively adjust the Voltage Source Converter (VSC) operation, ensuring stable DC link voltage despite fluctuations in renewable energy generation. This reduces reliance on feedback control and improves dynamic performance.

$$w_{PVff} = \frac{2P_{PV}}{3V_t} \tag{29}$$

$$w_{wff} = \frac{2P_{wind}}{3V_t} \tag{30}$$

Where, $P_{PV}$, $w_{PVff}$, $P_{wind}$, $w_{wff}$ are the wind power and its feed-forward term, photovoltaic power, and solar power, in that order. The d-component ($I_{Ld}$) and q-component ($I_{Lq}$) of the load current are both filtered to extract their respective DC components ($w_{dload}$ and $w_{qload}$) using a Moving Average Filter (MAF) to avoid any degradation in dynamic performance. The moving average filter is particularly effective in isolating the fundamental DC component while eliminating high-frequency noise. For both components, the MAF ensures a smooth extraction of the DC component, preserving the integrity of the current signals in the abc frame of reference. The transfer function of the moving average filter, which is applied to both the d-component and q-component, is characterized by its ability to average the signal over a specified window, reducing the impact of transient variations and harmonics. This method enables efficient and accurate extraction of the fundamental components from the load currents, ensuring the system's dynamic performance remains stable.

$$MAF = \frac{1-e^{-T_w S}}{T_w S} \tag{31}$$

For the moving average filter, $T_w$ stands for the window length. Since the dq-axis current contains a double harmonic component as its lowest harmonic, $T_w$ it is maintained at half the fundamental time period. The MAF's gain is one times the

window length in integers, and its DC gain is zero. The net active reference current can now be represented as

$$w_{total} = w_{loss} + w_{dload} - w_{wff} - w_{pvff} \quad (32)$$

The phase voltages ($V_{abc}$) are computed from the line voltages as

$$\begin{bmatrix} v_{sa} \\ v_{sb} \\ v_{sc} \end{bmatrix} = \frac{1}{3}\begin{bmatrix} 2 & 1 & 0 \\ -1 & 1 & 0 \\ -1 & -2 & 0 \end{bmatrix}\begin{bmatrix} v_{Lab} \\ v_{Lbc} \\ 0 \end{bmatrix} \quad (33)$$

$$V_t = \sqrt{\frac{2(V_{sa}^2+V_{Sb}^2+V_{sc}^2)}{3}} \quad (34)$$

$$u_{pa} = v_{sa} / V_t; u_{pb} = v_{sb} / V_t; u_{pc} = v_{sc} / V_t \quad (35)$$

$$u_{qa} = -\frac{u_{pb}}{\sqrt{3}} + \frac{u_{pc}}{\sqrt{3}}; u_{qb} = \frac{\sqrt{3}u_{pa}}{2} + \frac{(u_{pb}-u_{pc})}{2\sqrt{3}}; u_{qc} = -\frac{\sqrt{3}u_{pa}}{2} + \frac{(u_{pb}-u_{pc})}{2\sqrt{3}} \quad (36)$$

Line terminal voltage error represented as

$$V_{tc} = V_t^* - V_t \quad (37)$$

*5.2.3. Generation of Gate Pulses for VSC*

By multiplying its unit templates, the reference currents for source DG, which give power to the load at night, are finally produced.

$$i_{sa}^* = w_{total} \times u_{pa} + w_{total} \times u_{qa} \quad (38)$$

$$i_{sb}^* = w_{total} \times u_{pb} + w_{total} \times u_{qb} \quad (39)$$

$$i_{sc}^* = w_{total} \times u_{pc} + w_{total} \times u_{qc} \quad (40)$$

The top leg of the grid-side VSC comprises switches activated by gate pulses produced by a three-phase hysteresis relay. This relay receives the error between the reference currents and the observed currents from the grid voltage source converter. Using the complementary signal, the VSC of the bottom leg of the grid side is sent.

## 6. Bidirectional Dual Active Bridge (DAB) Converter Design for Electric Vehicle Fast Charging

A power electronics solution that allows bidirectional energy flow between the grid and Electric Vehicles (EVs) is a Wireless Bidirectional Dual Active Bridge (DAB) converter for rapid charging of electric vehicles. Figure 8 shows two active full bridges (one on the main side and one on the secondary side) coupled by a high-frequency transformer, therefore permitting bidirectional power flow for both charging and Vehicle-to-Gast (V2G) operation.

### *6.1. Basic Operation and Design of DAB*

The DAB converter works by converting DC power from the grid or a renewable source to AC, transmitting it through the transformer, and then converting it back to DC on the EV side. The primary and secondary sides of the converter are each controlled by a full-bridge of transistors operating at high switching frequencies. The voltage on each side is phase-shifted relative to the other, and this phase shift (ϕ) determines the direction and amount of power transferred. Power can flow in either direction: Grid to EV for charging or EV to Grid for energy feeding during V2G operations.

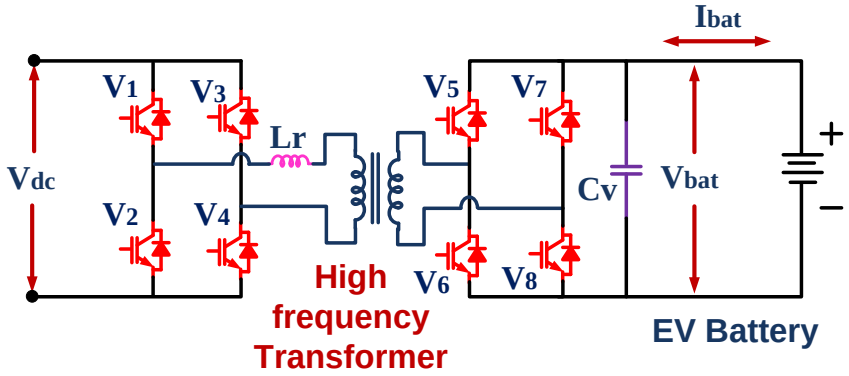


**Fig. 8 Dual active bridge converter for fast electric vehicle charging station**

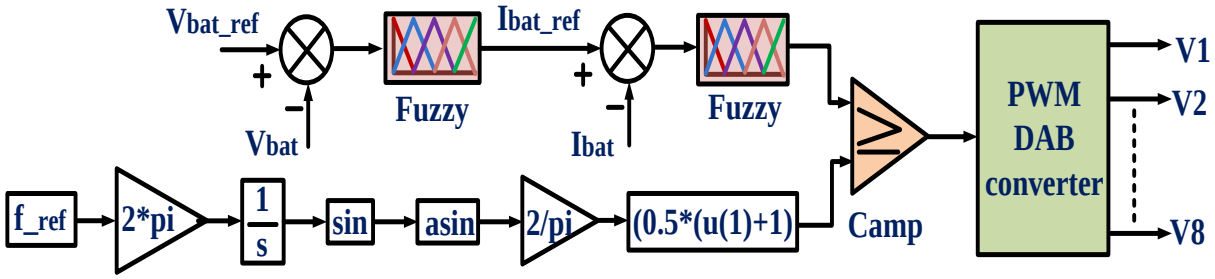


**Fig. 9 Controller design for dual active bridge converter for fast electric vehicle charging station**

### *6.2. Power Transfer in DAB*

The power transferred in the DAB converter can be expressed as:

$$P = \frac{n \cdot V_{Pri} \cdot V_{sec} \cdot \phi}{\omega L} \quad (41)$$

Where: P is the transferred power, n is the transformer turns ratio, $V_{Pri}$ is the primary side voltage, $V_{sec}$ is the secondary side voltage, ϕ is the phase shift between the primary and secondary voltages, ω is the switching angular frequency, L is the leakage inductance of the transformer. This equation shows how the phase shift between the primary and secondary side voltages governs the power transfer through the DAB converter. The inductance L is a critical factor in determining the power capacity and energy transfer rate.

### *6.3. High-Frequency Transformer*

A high-frequency transformer provides isolation between the two sides of the converter, allowing high-efficiency power transfer with galvanic isolation. In wireless power transfer systems, the transformer is replaced by inductive coupling. The key characteristics of the transformer include:

- Turns Ratio (n): The ratio between the primary and secondary windings determines the voltage conversion.
- Leakage Inductance (L): This determines the energy storage in the magnetic field and influences power transfer and losses.

### *6.4. Soft Switching for High Efficiency*

To minimize switching losses in the DAB converter, Zero Voltage Switching (ZVS) is employed, ensuring the transistors switch at zero voltage. This reduces power dissipation and increases efficiency, especially at high power levels.

The conditions for achieving ZVS are:

$$I_{load} > I_{mag} \quad (42)$$

Where: $I_{load}$ is the load current, $I_{mag}$ is the magnetizing current of the transformer. ZVS is critical in high-frequency converters to ensure soft switching, where switching transistors turn on/off with minimal losses.

### *6.5. Bidirectional Power Flow*

The DAB converter's bidirectional design lets electricity go from the grid to the EV for charging and from the EV back to the grid for V2G uses. The phase shift ϕ controls the direction of power flow; one may change this direction of energy transfer by adjusting ϕ.

- Forward Power Transfer (Grid to EV): Power flows from the grid to the EV, with a positive phase shift.
- Reverse Power Transfer (EV to Grid): Power flows back to the grid when the phase shift is negative.

### *6.6. Control and Modulation*

The control of the DAB converter is achieved through Phase-Shift Modulation (PSM), where the difference in phase between the two full bridges governs the power flow.

Advanced control algorithms adjust the phase shift for EV fast charging applications to maximize efficiency, regulate power flow, and manage the charging process. The transferred power can also be controlled using the duty cycle (D) of the switching transistors. The formula for output power considering duty cycle control is:

$$P_{out} = \frac{V_{in}^2 \cdot D \cdot (1-D)}{2 \cdot f_s \cdot L} \quad (43)$$

Where Vin is the input voltage, D is the duty cycle $f_s$ switching frequency, and L is the inductance.

### *6.7. Wireless Power Transfer*

In a wireless power transfer version of the DAB converter, the energy is transferred through inductive coupling between the primary and secondary coils instead of a physical transformer. The mutual inductance between the coils, M, is given by:

$$M = k\sqrt{L_1}L_2 \quad (44)$$

Where: k is the coupling coefficient; $L_1$ and $L_2$ are the self-inductances of the primary and secondary coils, respectively. The induced voltage in the secondary coil, due to mutual inductance, is:

$$V_{sec} = j\omega M I_{Pri} \quad (45)$$

A wireless power transfer system's secondary coil voltage is governed by this equation, which is proportional to the main coil current and the mutual inductance of the two coils. For fast EV charging, the DAB converter operates at high power levels (typically 50 kW or more).

The wireless version eliminates physical connectors, reducing wear and tear and improving user convenience. It provides a high level of efficiency, bidirectional capability, and soft switching, making it ideal for modern EV charging stations.

## 7. Neutral Point Clamped Bidirectional Voltage Source Converter Design

In an Neutral-Point-Clamped (NPC) converter used in an Electric Vehicle (EV) charging station, the converter ensures efficient AC-DC and DC-AC conversion while maintaining high power quality.

The three-level NPC topology is commonly applied due to its ability to handle higher voltages with reduced Total Harmonic Distortion (THD), making it ideal for charging stations, as shown in Figure 10.

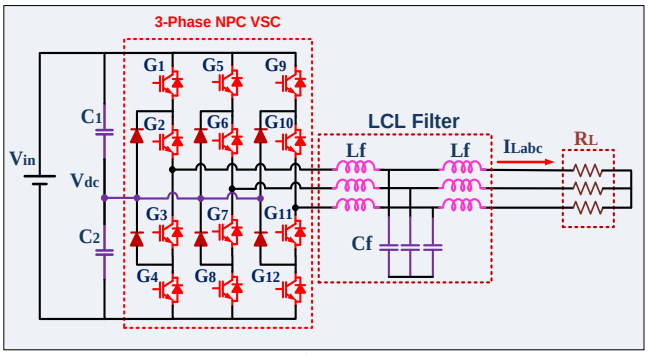


**Fig. 10 Schematic diagram of NPC voltage sources converter**

### *7.1. Phase Voltage Equations (Three-Phase NPC Converter)*

The converter generates three levels of output voltage: $+\frac{V_{dc}}{2}$, 0 and $-\frac{V_{dc}}{2}$

For each phase (a, b, and c):

$$V_{an} = \frac{V_{dc}}{2} \cdot s_a \tag{46}$$

$$V_{bn} = \frac{V_{dc}}{2} \cdot s_b \tag{47}$$

$$V_{cn} = \frac{V_{dc}}{2} \cdot s_c \tag{48}$$

Where: $V_{an}$,$V_{bn}$,$V_{cn}$ are the phase-to-neutral voltages, $s_a$, $s_b$, $s_c$ are the switching functions for each phase and take values of +1, 0, or −1 depending on the switch states, $V_{dc}$ is the DC-link voltage.

### *7.2. Neutral Point Voltage Equation*

The neutral-point voltage drift is a critical issue in NPC converters. The neutral-point current must be balanced to avoid voltage unbalance in the capacitors. For the neutral-point voltage $V_{nP}$, the following equation holds:

$$V_{\mathrm{nP}} = \frac{V_{c1} - V_{c2}}{2} \tag{49}$$

Where: $V_{C1}$ and $V_{C2}$ are the voltages across the upper and lower capacitors of the DC-link.

### *7.3. Neutral-Point Current*

The neutral-point current $I_{nP}$ is defined as the current flowing through the neutral point and depends on the imbalance in switching.

$$I_{nP} = I_{upper} - I_{lower} \tag{50}$$

Where: $I_{upper}$ is the current through the upper switches, $I_{lower}$ is the current through the lower switches. The neutral-point current must be controlled to ensure that $I_{nP}$ = 0 to avoid drift in the neutral-point voltage.

### *7.4. AC to DC Conversion Equations*

For the AC-DC conversion process in the NPC converter, the output DC voltage $V_{dC}$ is related to the input AC voltage $V_{in}$ as follows:

$$V_{dc} = \frac{3\sqrt{2}}{\pi} V_{in} \tag{51}$$

Where: $\mathrm{V_{in}}$ is the RMS value of the input AC voltage. The DC current $I_{dC}$ is related to the AC current $I_{in}$ as:

$$I_{dc} = \frac{3\sqrt{2}}{\pi} I_{in} \tag{52}$$

Where: $V_{in}$ is the RMS value of the input AC voltage

### *7.5. Power Flow Equations*

The power delivered from the AC side to the DC side during charging is given by:

$$P_{AC} = 3V_{in}I_{in}\cos(\phi) \tag{53}$$

Where: $P_{AC}$ is the active power transferred from the grid to the EV, $V_{in}$ is the phase voltage, $I_{in}$ is the phase current, $\cos(\phi)$ is the power factor. The power on the DC side of the converter can be expressed as:

$$P_{DC} = V_{dC}I_{dC} \tag{54}$$

### *7.6. Total Harmonic Distortion (THD) Calculation*

The NPC converter is designed to reduce THD. The formula to calculate THD in the output current is:

$$THD = \sqrt{\frac{\sum_{n=2}^{\infty} I_n^2}{I_1^2}} \times 100 \tag{55}$$

Where $I_n$ is the RMS value of the nth harmonic current, $I_1$ is the RMS value of the fundamental current.

### *7.7. DC-Link Capacitor Design Equation*

The size of the DC-link capacitor in an NPC converter is crucial for maintaining stable voltage. The required capacitance $C_{dc}$ can be calculated as:

$$C_{dc} = \frac{P_{DC}}{2 \cdot f_{sw} \cdot \Delta V_{dc} \cdot V_{dc}} \tag{56}$$

Where: $P_{DC}$ is the DC power, $f_{sw}$ is the switching frequency, $\Delta V_{dc}$ is the allowable ripple in the DC-link voltage.

### *7.8. Inductor Design (Ripple Filter)*

The inductor value is designed based on the allowed current ripple and switching frequency. The formula is:

$$L = \frac{V_{dc} \cdot D \cdot (1-D)}{f_s \cdot \Delta I_{ripple}} \tag{57}$$

Where: L = Inductor value (in Henrys), $\mathrm{V_{dc}}$ = DC bus voltage (in Volts), D = Duty cycle (ratio between 0 and 1), $f_s$ = Switching frequency (in Hertz), $\Delta I_{ripple}$ = Allowed peak-to-peak current ripple (in Amperes)

### *7.9. Capacitor Design (Ripple Filter)*

The capacitor value is chosen based on the desired voltage ripple and the current flowing through the capacitor. The formula is:

$$c = \frac{I_{load}}{4 \cdot f_s \cdot V_{ripple}} \tag{58}$$

Where C = Capacitor value (in Farads), $I_{load}$ = load current (in Amperes), $f_s$ = Switching frequency (in Hertz), $V_{ripple}$ = Allowed peak-to-peak voltage ripple (in Volts).

## 8. Proposed Fuzzy Logic Controller Design

The control of DC link voltage ($V_{dC}$) is crucial for system stability and efficient power flow, especially in grid-connected systems or renewable energy integration scenarios, as shown in Figure 11. The process starts with generating a reference DC link voltage ($V_{dC}^{*}$) determined by the DC link voltage controller based on operational requirements. The actual DC link voltage is continuously monitored and compared to the reference value to produce a voltage error ($V_{dce} = V_{dc}^{*} - V_{dc}$), which serves as the primary input for corrective action.

The rate of change in the voltage error ($\Delta V_{dce}$) is also calculated to enhance the control process's accuracy. Both the voltage error and its change are fed into the fuzzy logic controller (FLC), which plays a vital role in addressing system nonlinearities and uncertainties. The FLC intelligently adjusts the control action based on predefined rules and membership functions, resulting in a compensated error signal ($V_{dce\_flc}$) and a modified error signal ($V_{dc\_mod}$). This modified error is then passed to the main voltage controller, which adjusts power electronics to regulate the DC link voltage accordingly. This hybrid control strategy enhances the performance of the DC link voltage control system by reducing overshoot, improving transient response, and maintaining voltage stability under varying operational conditions.

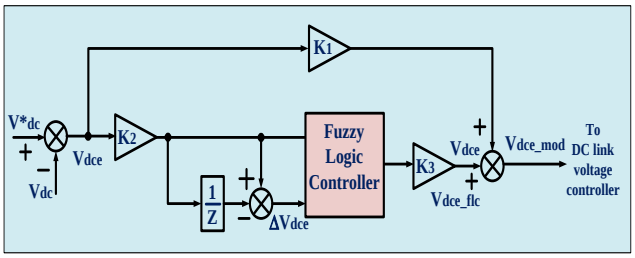


**Fig. 11 Schematic diagram of hybrid fuzzy DC link voltage controller**

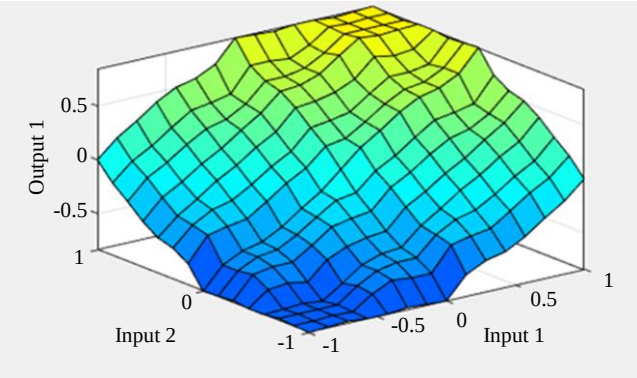


**Fig. 12 Surface view of rule Base for FLC**

## 9. Results and Discussion

### *9.1. Wind Grid Connected Renewable Energy System for Stability and Load Balancing with Fuzzy Logic Control*

For power stability and quality, fuzzy logic control optimises solar and wind energy integration in this grid-connected electric vehicle rapid charging system. Local linear and nonlinear loads and EV charging stations are driven by a 60-kW solar array and wind turbine electricity. The nonlinear load is 10 kW; the linear load is 100 kW; the EV charging station runs 30 kW. The total load demand is 140 kW, more than the capacity of 120 kW renewable energy-producing capabilities.

The grid must provide the remaining 20 kW to balance the load. Fuzzy logic controls smooth variations in renewable energy output brought on by weather. Variations in the production of solar and wind power influence the energy supply. Figure 12 illustrates the wind turbine produces 30 kW instead of 60 kW when the wind speed lowers from 12 m/s to 10 m/s between 0.2 seconds and 0.8 seconds.

Loss of wind generation lowers demand and EV charging energy, pushing grid reliance to offset the gap. Furthermore, after 0.3–0.7 seconds, solar irradiation falls from 1000 W/m² to 500 W/m², therefore changing the solar power production from 60 kW to 30 kW. This aggravates the power scarcity; hence, grid support becomes even more important.

The EV charging current swings from 50 A to 100 A between 0.4 and 0.6 seconds, therefore extracting more power for quick charging. This increase in EV charging demand matches a decrease in renewable energy supply; hence, more grid power is needed to charge EVs without upsetting other needs.

Dynamic power distribution among loads, renewable sources, and the grid lets the fuzzy logic controller optimise system stability under changing circumstances. As shown by power flow fluctuations in Figure 13, the controller reduces voltage fluctuations and maintains grid current quality, hence preserving power quality. This method lowers THD, balances load demand, and improves the EV charging infrastructure created from renewable energy sources.

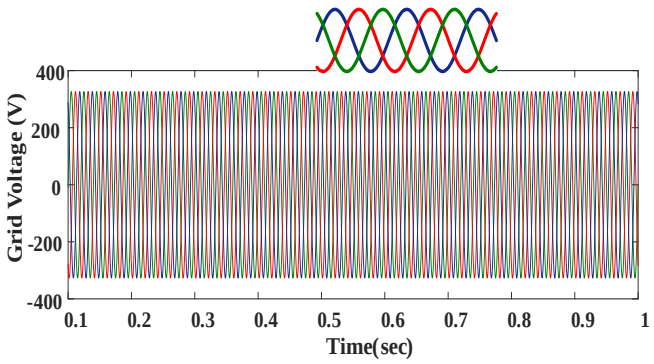

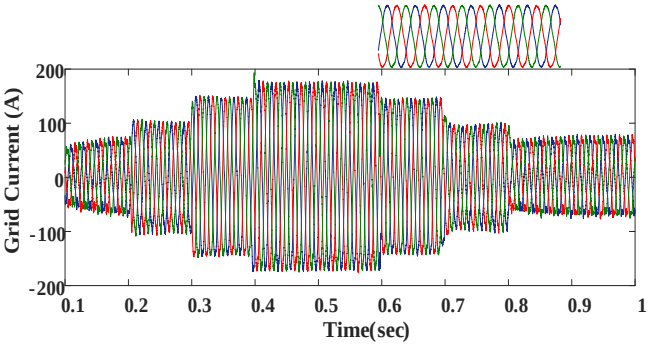
Grid Current (A)
Time(sec)

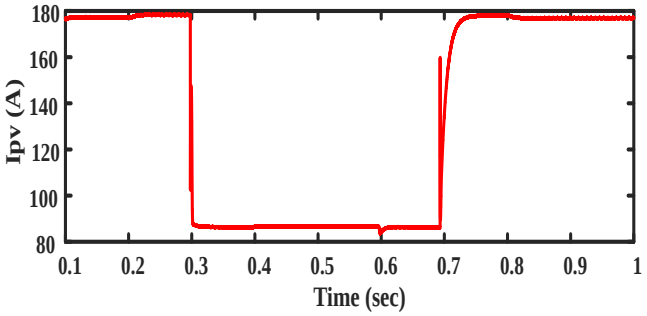
Ipv (A)
Time (sec)

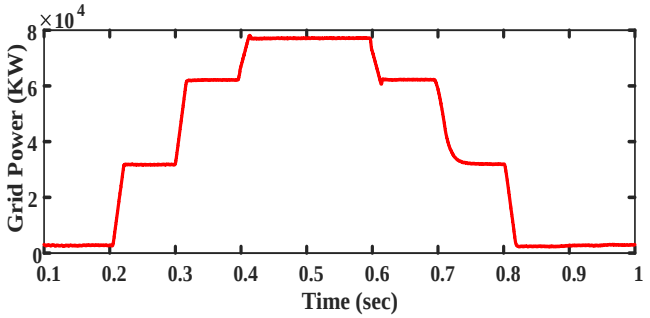
Grid Power (KW)
Time (sec)

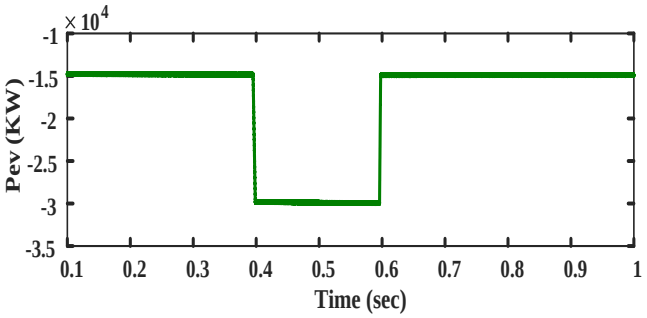
Pev (KW)
Time (sec)

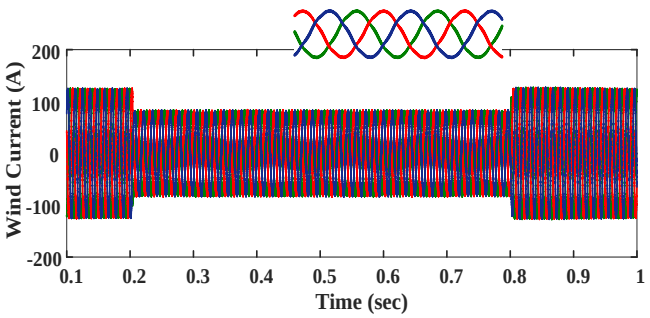
Wind Current (A)
Time (sec)

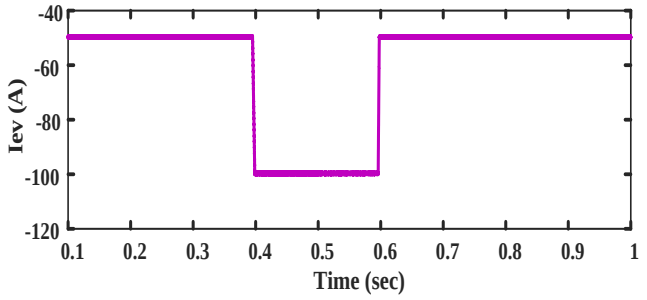
Iev (A)
Time (sec)

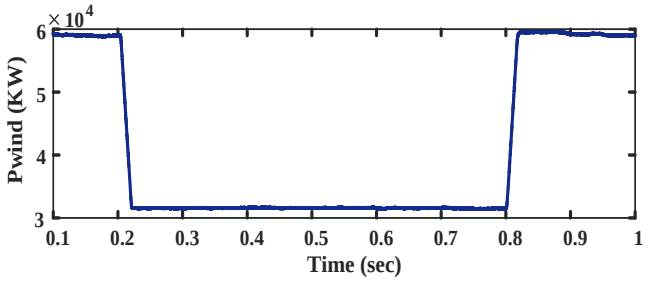
Pwind (KW)
Time (sec)

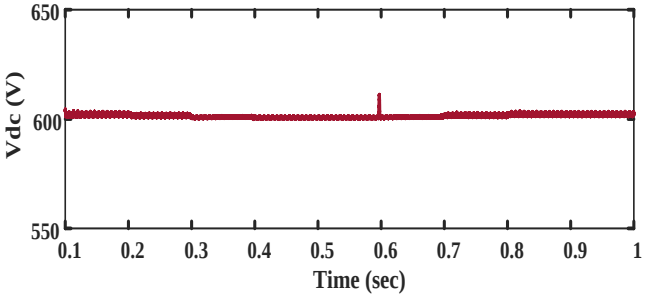
Vdc (V)
Time (sec)

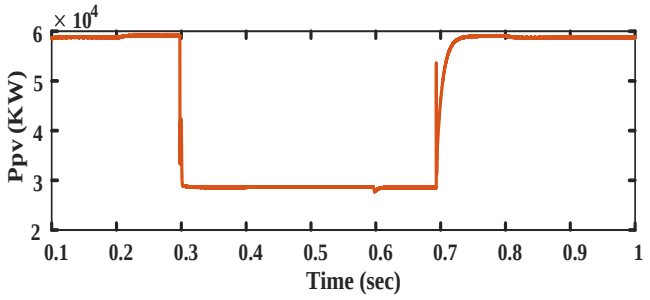
Ppv (KW)
Time (sec)

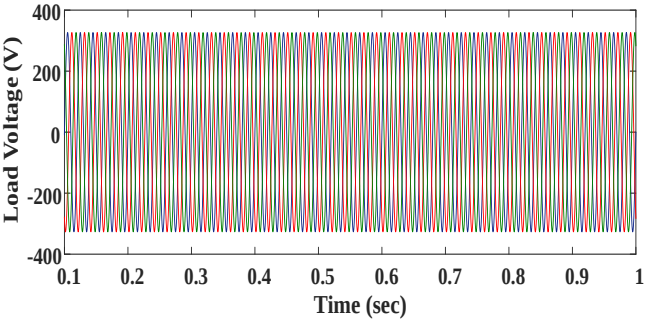
Load Voltage (V)
Time (sec)

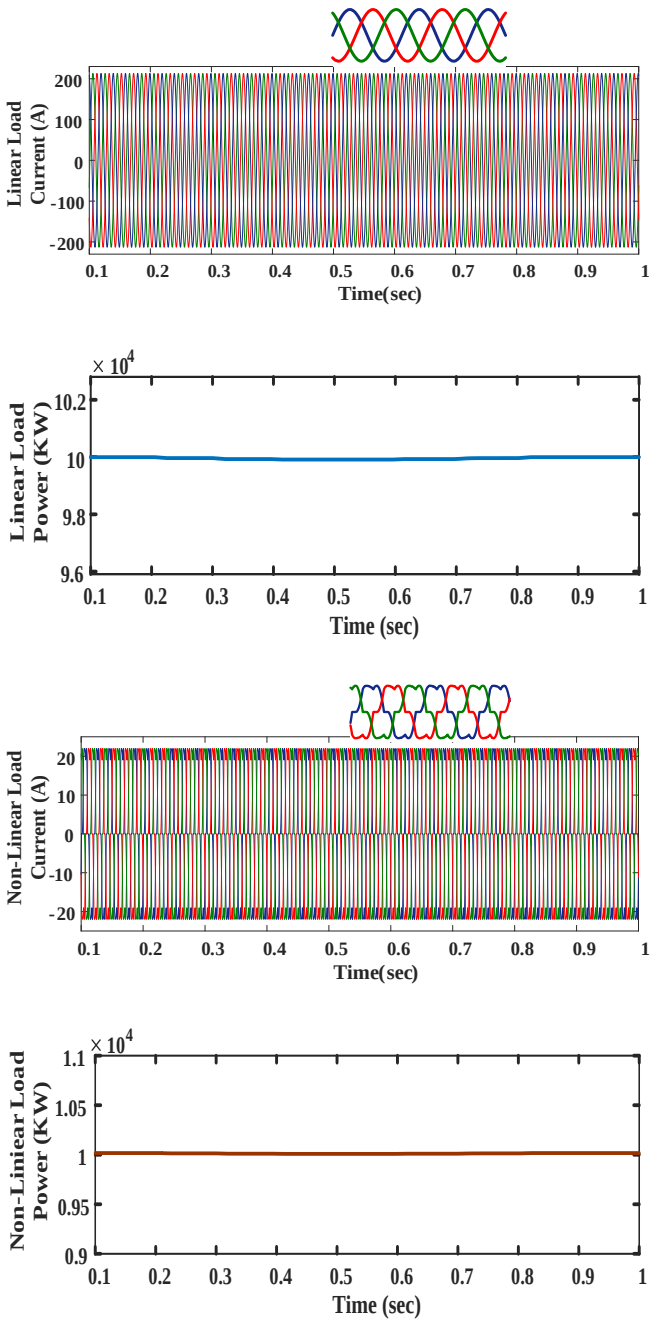


**Fig. 13 Simulation results of grid-connected renewable energy system for stability and load balancing with fuzzy logic control**

### *9.2. Comparative Results of Fuzzy and PI Controller Technique*

Solar and wind energy combined into grid-connected Electric Vehicle (EV) quick charging stations will help to increase stability and power quality. To improve the efficiency of this integration, we have replaced traditional Proportional Integral (PI) control strategies with a Fuzzy Logic Controller (FLC). Though the PI controller is usually used for system control, it usually fails to respond to the dynamic changes in power supply and load demand, particularly in fast fluctuations in renewable energy generation. Conversely, the Fuzzy Logic Controller uses a more flexible approach by way of a rule-based system capable of effectively controlling uncertain and variable circumstances. This flexibility enables the FLC to limit dynamic and transient responses, retaining system stability and improving power quality. As demonstrated in Figure 14, the performance of the fuzzy controller far surpasses that of the PI controller, especially in the management of changes linked to renewable energy sources.

This progress not only guarantees the optimal use of renewable energy sources but also increases the reliability of the infrastructure for EV charging. Maintaining system performance and stability in grid-connected Electric Vehicle (EV) quick charging systems employing solar and wind energy relies significantly on power quality. Among the key power quality measures in both grid and load currents is their Total Harmonic Distortion (THD). The Fuzzy Logic Controller (FLC) over the Proportional-Integral (PI) controller considerably improves these values. In Figures 14(a) and (c), the grid current THD with the FLC is dropped to 2.3%, a notable decrease over the 3.75% THD recorded with the PI controller.

Moreover, under non-linear load conditions, the FLC gets a non-linear load current THD of 19.27%, as shown in Figure 14(d), whereas the PI controller generates a larger THD of 22.14%, as shown in Figure 14(c). These results demonstrate the remarkable potential of the FLC to reduce harmonic distortion, therefore maximising power quality, improving system stability, and ensuring more efficient integration of renewable energy sources with the grid and EV charging infrastructure.

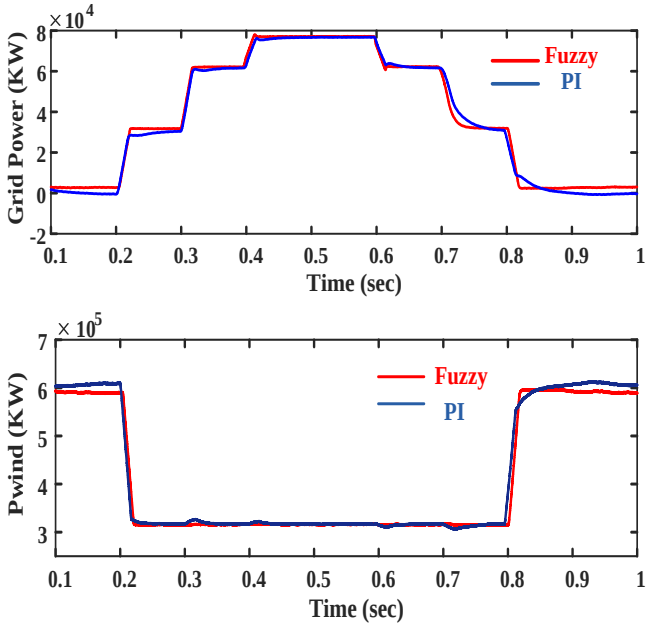

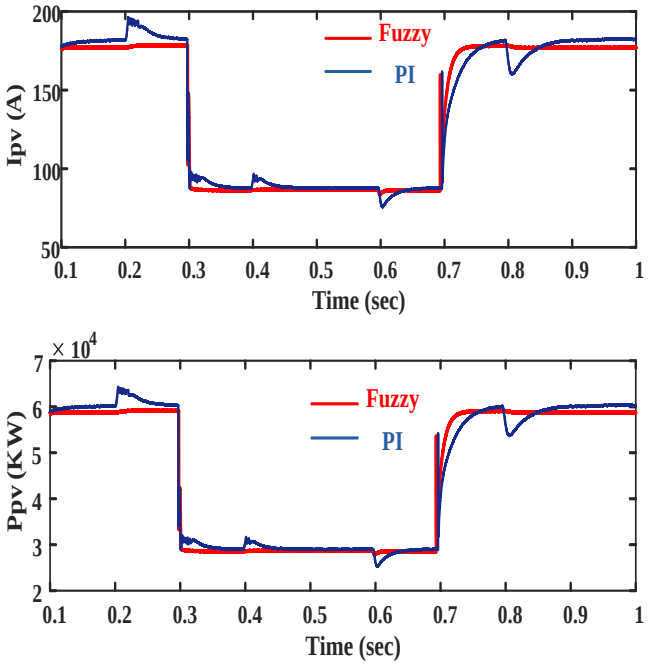


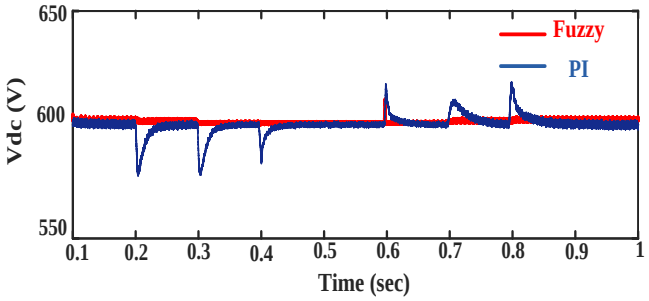


**Fig. 14 Simulation results of comparative fuzzy and PI control technique**

**Table 1. Comparison details of fuzzy and PI controller**

| Parameters | Fuzzy | PI |
|---|---|---|
| Rise Time (s) | 0.0072 | 0.0042 |
| Settling Time (s) | 0.0186 | 0.0657 |
| Peak Time (s) | 0.0109 | 0.0176 |
| Overshoot Time(ms) | 56.0887 | 92.7743 |
| Peak (V) | 931.8202 | 1157 |
| Grid current THD (%) | 2.3 | 3.75 |
| Load current THD (%) | 19.27 | 22.14 |

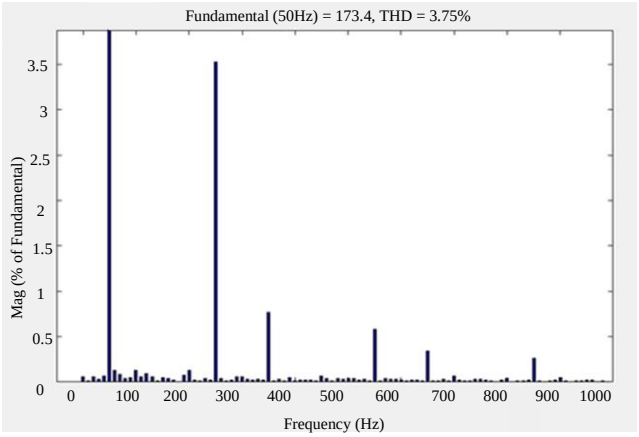


(a)

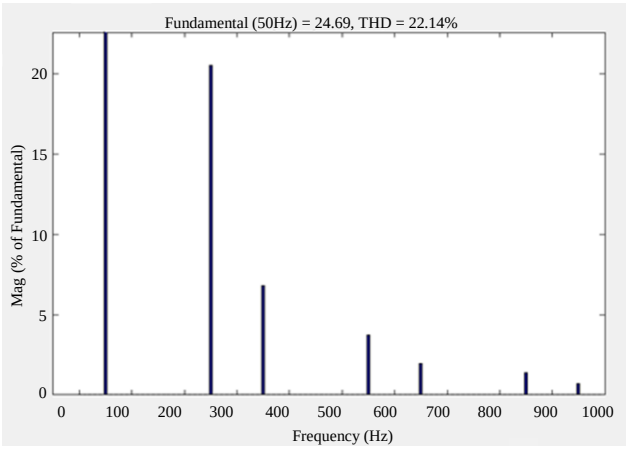


(b)

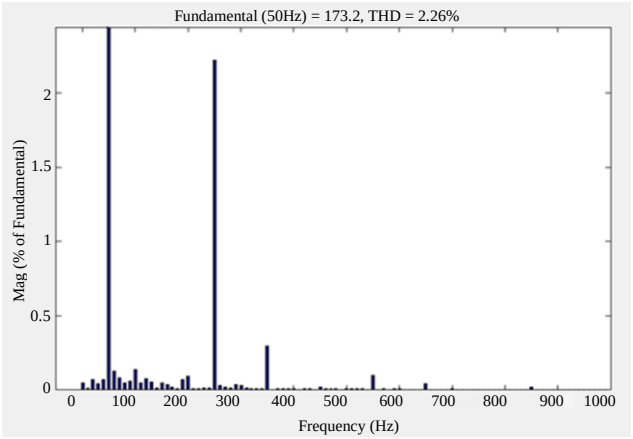


(c)

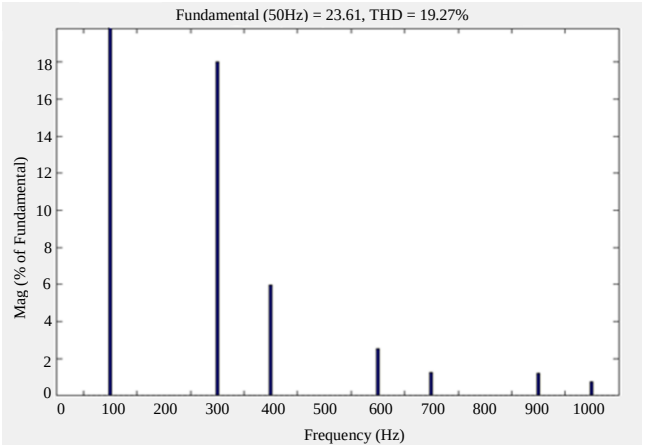


(d)

**Fig. 15 Comparative results for grid and load current THD values**

## 10. Conclusion

The proposed system improves system reliability and energy economy by effectively merging solar and wind energy sources into a grid-connected Electric Vehicle (EV) fast-charging configuration. Maximum Power Point Tracking (MPPT) for optimal energy extraction and Neutral-Point Clamped (NPC) converters for increased voltage balancing guarantee smooth power management in the system. Particularly by reducing Total Harmonic Distortion (THD) in both grid current and nonlinear load conditions, the acceptability of a Fuzzy Logic Controller (FLC) has far surpassed the standard PI controller regarding stability and power quality. By way of its dynamic reactivity to variations in power production and load demand, the FLC protects system stability and improves the overall performance of the integrated system. These innovative technologies, taken together, enable the system to handle household load management, fast EV charging, and complex renewable energy integration, therefore offering a solid and scalable solution for future energy demands. Apart from encouraging sustainable energy use, this approach ensures a great level of power quality and operational efficiency.

## References


[1] Benjamin Kroposki, Pankaj K. Sen, and Keith Malmedal, "Selection of Distribution Feeders for Implementing Distributed Generation and Renewable Energy Applications," *IEEE Transactions on Industry Applications*, vol. 49, no. 6, pp. 2825-2834, 2013. [CrossRef] [Google Scholar] [Publisher Link]

[2] Bei Han et al., "Paths Toward Smart Energy: A Framework for Comparison of the EU and China Energy Policy," *IEEE Transactions on Sustainable Energy*, vol. 5, no. 2, pp. 423-433, 2014. [CrossRef] [Google Scholar] [Publisher Link]

[3] Meng Liu, Wei-Jen Lee, and Lyndon K. Lee, "Financial Opportunities by Implementing Renewable Sources and Storage Devices for Households Under ERCOT Demand Response Programs Design," *IEEE Transactions on Industry Applications*, vol. 50, no. 4, pp. 2780 2787, 2014. [CrossRef] [Google Scholar] [Publisher Link]

[4] Benjamin Kroposki, Pankaj K. Sen, and Keith Malmedal, "Optimum Sizing and Placement of Distributed and Renewable Energy Sources in Electric Power Distribution Systems," *IEEE Transactions on Industry Applications*, vol. 49, no. 6, pp. 2741-2752, 2013. [CrossRef] [Google Scholar] [Publisher Link]

[5] Olawale Ogunrinde, Ekundayo Shittu, and Kanwalroop Kathy Dhanda, "Investing in Renewable Energy: Reconciling Regional Policy with Renewable Energy Growth," *IEEE Engineering Management Review*, vol. 46, no. 4, pp. 103-111, 2018. [CrossRef] [Google Scholar] [Publisher Link]

[6] Shailendra Kumar Tiwari, Bhim Singh, and Puneet Kr. Goel, "Design and Control of Microgrid Fed by Renewable Energy Generating Sources," *IEEE Transactions on Industry Applications.*, vol. 54, no. 3, pp. 2041-2050, 2018. [CrossRef] [Google Scholar] [Publisher Link]

[7] "1547-2003 - IEEE Standard for Interconnecting Distributed Resources with Electric Power Systems," *IEEE*, pp. 1-28, 2003. [CrossRef] [Google Scholar] [Publisher Link]

[8] Ahmad G. Abd-Elkader, Saber M. Saleh, and M. B. Magdi Eiteba, "A Passive Islanding Detection Strategy for Multi-Distributed Generations," *International Journal of Electrical Power & Energy Systems*, vol. 99, pp. 146-155, 2018. [CrossRef] [Google Scholar] [Publisher Link]

[9] Salman Habib, Muhammad Kamran, and Umar Rashid, "Impact Analysis of Vehicle-Togrid Technology and Charging Strategies of Electric Vehicles on Distribution Networks-A Review," *Journal of Power Sources*, vol. 277, pp. 205-214, 2015. [CrossRef] [Google Scholar] [Publisher Link]

[10] Felix Garcia-Torres et al., "Optimal Management of Microgrids with External Agents Including Battery/Fuel Cell Electric Vehicles," *IEEE Transactions on Smart Grid*, vol. 10, no. 4, pp. 4299-4308, 2019. [CrossRef] [Google Scholar] [Publisher Link]

[11] Sid-Ali Amamra, and James Marco, "Vehicle-To-Grid Aggregator to Support Power Grid and Reduce Electric Vehicle Charging Cost," *IEEE Access*, vol. 7, pp. 178528-178538, 2019. [CrossRef] [Google Scholar] [Publisher Link]

[12] Chunhua Liu et al., "Opportunities and Challenges of Vehicle-To-Home, Vehicle-To-Vehicle, and Vehicle-To-Grid Technologies," *Proceedings of the IEEE*, vol. 101, no. 11, pp. 2409-2427, 2013. [CrossRef] [Google Scholar] [Publisher Link]

[13] Moacyr Aureliano Gomes de Brit et al., "Evaluation of the Main MPPT Techniques for Photovoltaic Applications," *IEEE Transactions on Industrial Electronics*, vol. 60, no. 3, pp. 1156-1167, 2013. [CrossRef] [Google Scholar] [Publisher Link]

[14] Weidong Xiao et al., "Overview of Maximum Power Point Tracking Technologies for Photovoltaic Power Systems," *IECON 2011 - 37th Annual Conference of the IEEE Industrial Electronics Society*, Melbourne, VIC, Australia, pp. 3900-3905, 2011. [CrossRef] [Google Scholar] [Publisher Link]

[15] Jubaer Ahmed, and Zainal Salam, "An Enhanced Adaptive P&O MPPT for Fast and Efficient Tracking under Varying Environmental Conditions," *IEEE Transactions on Sustainable Energy*, vol. 9, no. 3, pp. 1487-1496, 2018. [CrossRef] [Google Scholar] [Publisher Link]

[16] Rachid Errouissi, and Ahmed Al-Durra, "A Novel PI-Type Sliding Surface for PMSG-Based Wind Turbine with Improved Transient Performance," *IEEE Transactions on Energy Conversion*, vol. 33, no. 2, pp. 834-844, 2018. [CrossRef] [Google Scholar] [Publisher Link]

[17] Satyajit Das, and Bidyadhar Subudhi, "A $H_\infty$ Robust Active and Reactive Power Control Scheme for a PMSG-Based Wind Energy Conversion System," *IEEE Transactions on Energy Conversion*, vol. 33, no. 3, pp. 980-990, 2018. [CrossRef] [Google Scholar] [Publisher Link]

[18] Shihua Li, Mingming Zhou and Xinghuo Yu, "Design and Implementation of Terminal Sliding Mode Control Method for PMSM Speed Regulation System," *IEEE Transactions on Industrial Informatics*, vol. 9, no. 4, pp. 1879- 1891, 2013. [CrossRef] [Google Scholar] [Publisher Link]

[19] Rachid Errouissi, Ahmed Al-Durra, and Mahdi Debouza, "A Novel Design of PI Current Controller for PMSG-Based Wind Turbine Considering Transient Performance Specifications and Control Saturation," *IEEE Transactions on Industrial Electronics*, vol. 65, no. 11, pp. 8624-8634, 2018. [CrossRef] [Google Scholar] [Publisher Link]

[20] Akira Nabae, Isao Takahashi, and Hirofumi Akagi, "A New Neutral-Point-Clamped PWM Inverter," *IEEE Transactions on Industry Applications*, vol. IA-17, pp. 518-523, 1981. [CrossRef] [Google Scholar] [Publisher Link]

[21] Guo Chen et al., "Compensation Voltage Injection Based Neutral Point Voltage Fluctuation Suppression for NPC Converter," *Proceedings of the 2022 Asia Power and Electrical Technology Conference (APET)*, Shanghai, China, pp. 203-208, 2022. [CrossRef] [Google Scholar] [Publisher Link]

[22] Peng Liu et al., "A Double ModulationWave CBPWM Strategy Providing Neutral-Point Voltage Oscillation Elimination and CMV Reduction for Three-Level NPC Inverters," *IEEE Transactions on Industrial Electronics*, vol. 65, no. 1, pp. 16-26, 2018. [CrossRef] [Google Scholar] [Publisher Link]

[23] Oghenewvogaga Oghorada et al., "Inter-cluster Voltage Balancing Control of Modular Multilevel Cascaded Converter Under Unbalanced Grid Voltage," *Journal of Modern Power Systems and Clean Energy*, vol. 10, no. 2, pp. 515-523, 2022. [CrossRef] [Google Scholar] [Publisher Link]

[24] Chelladurai Balasundar et al., "Mixed Step Size Normalized Least Mean Fourth Algorithm of DSTATCOM Integrated Electric Vehicle Charging Station," *IEEE Transactions on Industrial Informatics*, vol. 19, no. 6, pp. 7583-7591, 2023. [CrossRef] [Google Scholar] [Publisher Link]

[25] Dennis van der Meer, "Energy Management System with PV Power Forecast to Optimally Charge EVs at the Workplace," *IEEE Transactions on Industrial Informatics*, vol. 14, no. 1, pp. 311-320, 2018. [CrossRef] [Google Scholar] [Publisher Link]

[26] Rik W.A.A. De Doncker, Deepakraj M. Divan, and Mustansir H. Kheraluwala, "A Three-Phase Soft-Switched High-Power-Density DC/DC Converter for High-Power Applications," *IEEE Transactions on Industry Applications*, vol. 27, no. 1, pp. 63-73, 1991. [CrossRef] [Google Scholar] [Publisher Link]

[27] Rejaul Islam, S M Sajjad Hossain Rafin, and Osama A. Mohammed, "Comprehensive Review of Power Electronic Converters in Electric Vehicle Applications," *Forecasting*, vol. 5, no. 1, pp. 22-80, 2022. [CrossRef] [Google Scholar] [Publisher Link]

[28] Donglai Liang, Jian Li, and Ronghai Qu, "Sensorless Control of Permanent Magnet Synchronous Machine Based on Second-Order Sliding-Mode Observer with Online Resistance Estimation," *IEEE Transactions on Industry Applications*, vol. 53, no. 4, pp. 3672-3682, 2017. [CrossRef] [Google Scholar] [Publisher Link]

[29] Mahammad A. Hannan et al., "Quantum-Behaved Lightning Search Algorithm to Improve Indirect Field-Oriented Fuzzy-PI Control for IM Drive," *IEEE Transactions on Industry Applications*, vol. 54, no. 4, pp. 3793-3805, 2018. [CrossRef] [Google Scholar] [Publisher Link]

[30] Shadab Murshid, and Bhim Singh, "Simulation and Hardware Implementation of PMSM Driven Solar Water Pumping System," *2018 International Conference on Power, Instrumentation, Control and Computing (PICC)*, Thrissur, India, pp. 1-6, 2018. [CrossRef] [Google Scholar] [Publisher Link]

[31] Younggi Lee, and Seung-Ki Sul, "Model-Based Sensorless Control of an IPMSM With Enhanced Robustness Against Load Disturbances Based on Position and Speed Estimator Using a Speed Error," *IEEE Transactions on Industry Applications*, vol. 54, no. 2, pp. 1448-1459, 2018. [CrossRef] [Google Scholar] [Publisher Link]

[32] Danyang Bao et al., "Adaptive Synchronous-Frequency Tracking-Mode Observer for the Sensorless Control of a Surface PMSM," *IEEE Transactions on Industry Applications*, vol. 54, no. 6, pp. 6460-6471, 2018. [CrossRef] [Google Scholar] [Publisher Link]

[33] Liu Sheng, Guo Xiaojie and Zhang Lanyong, "Robust Adaptive Backstepping Sliding Mode Control for Six-Phase Permanent Magnet Synchronous Motor Using Recurrent Wavelet Fuzzy Neural Network," *IEEE Access*, vol. 5, pp. 14502-14515, 2017. [CrossRef] [Google Scholar] [Publisher Link]

[34] Hadi Zayyani, "Continuous Mixed P-Norm Adaptive Algorithm for System Identification," *IEEE Signal Processing Letters*, vol. 21, no. 9, pp. 1108-1110, 2014. [CrossRef] [Google Scholar] [Publisher Link]

[35] Long Shi, Haiquan Zhao, and Yuriy Zakharov, "Generalized Variable Step Size Continuous Mixed P-Norm Adaptive Filtering Algorithm," *IEEE Transactions on Circuits and Systems II: Express Briefs*, vol. 66, no. 6, pp. 1078-1082, 2019. [CrossRef] [Google Scholar] [Publisher Link]

[36] Farheen Chishti, Shadab Murshid, and Bhim Singh, "PCC Voltage Quality Restoration Strategy of An Isolated Microgrid Based on Adjustable Step Adaptive Control," *2020 IEEE International Conference on Power Electronics, Smart Grid and Renewable Energy (PESGRE 2020)*, Cochin, India, pp. 1-6, 2020. [CrossRef] [Google Scholar] [Publisher Link]